Ca pillar effect on the electrochemistry and stability of P2-$Na_xCa_yFe_{0.5}Mn_{0.5}O_2$ for sodium-ion batteries

Yikang Jing[1,†] Haonan Wang[1,†], Anthony T. Pacileo[1], Nathanael Strong[1], Linna Qiao[1], Guangwen Zhou[1,2], Hao Liu[1,3]*

[1] Materials Science and Engineering Program, Binghamton University, Binghamton, New York, 13902, United States

[2] Department of Mechanical Engineering, Binghamton University, Binghamton, New York, 13902, United States

[3] Department of Chemistry, Binghamton University, Binghamton, New York, 13902, United States

KEYWORDS. Pillar effect, sodium-ion battery.

† Equal contribution

ABSTRACT. Cationic substitution at the Na site in the layered transition metal oxides creates a pillar effect that enhances the stability and electrochemical performance of sodium-ion battery cathodes. However, the conventional solid-state synthesis method for such substitution is often plagued by non-uniform elemental distribution or phase segregation, limiting the application and understanding of the pillaring effect. In this study, we synthesized a series of P2-type $Na_xCa_yFe_{0.5}Mn_{0.5}O_2$ materials via a solid-state ion exchange method, achieving controlled incorporation of Ca^{2+} at the Na sites. Structural analysis confirms successful Ca substitution and uniform distribution. Ca substitution reduces the lattice mismatch for the phase transitions during electrochemical cycling. Electrochemical testing reveals that Ca substitution decreases reversible capacity without significant improvement in capacity retention. Furthermore, Ca-substituted samples demonstrate enhanced resistance to degradation under air, water, and moist CO_2 exposure. These findings highlight the pillaring effects induced by Ca, which provide insights into designing more durable cathode materials for sodium-ion batteries.

I. INTRODUCTION

Sodium-ion batteries (SIBs) have become a competitive alternative to Li-ion batteries thanks to the abundance of sodium and the ease of Na ion intercalation in various host lattices [1]. One promising class of cathode materials for SIBs is the layered transition metal oxides, which afford rich transition metal composition, high capacity and voltage, and scalable synthesis [2]. However, sodium layered transition metal oxides are susceptible to degradation when exposed to air [3–5], which poses challenges for materials storage and processing [6]. The (de)intercalation of Na ions also induces detrimental layer-gliding phase transitions that limit the practical reversible capacity [7,8]. Overcoming these challenges is important to unlock the full potential of Na-ion battery chemistry.

Elemental substitution is a popular strategy to modify material properties for improved performance. For the layered transition metal oxides, the conventional approach is focused on the cationic substitution at the transition metal sites, which can be carried out with elements of diverse chemistries. For example, elements from both within and outside the transition metal series have been substituted at the transition metal sites with great success [9–13]. Recently, ionic potential [14,15] has been introduced to guide the cationic substitution strategy for the rational design of high-performance layered cathode materials.

An alternative cationic substitution approach is through substitution at the alkali metal sites (i.e., Na sites). A popular application of this approach is to substitute a larger cation (e.g., K^+) than Na^+ at the alkali metal sites [16,17], creating the so-called "pillar effect" that usually results in improved electrochemical performance. The "pillar effect" typically manifests in expanded interlayer spacing to facilitate ion diffusion and in the suppressed volume change or lattice mismatch upon phase transition. In contrast, attempts to substitute with a smaller cation often led to phase segregation due to the size disparity with Na^+ [18,19]. Substitution with ions of similar size to Na^+ generally resorts to the divalent Ca^{2+} cation [20–25], which has been shown to improve both the electrochemical cycling behavior and the stability of the layered cathode under various storage conditions. While the similar ionic size of Na^+ and Ca^{2+} is expected to favor a uniform mixing of Ca and Na at all ratios, the solid-state synthesis method to substitute Na with Ca usually results in secondary phases when the Ca concentration is above a few atomic percent [24,26] or a non-uniform Ca distribution even at a low doping level [22]. This raises the question of whether and how lattice-level Ca substitution can be achieved and how the concentration of Ca affects the properties and behavior of the layered materials.

In this work, we have used an ion exchange method to substitute Na with Ca in the P2-$Na_{0.67}Fe_{0.5}Mn_{0.5}O_2$ cathode material to study the effect of Ca substitution on electrochemistry and storage stability. The P2-$Na_{0.67}Fe_{0.5}Mn_{0.5}O_2$ operates by a combination of the transition metal ion redox and the anionic redox of the lattice oxygen [27–29]. The high-voltage process exhibits voltage hysteresis and is accompanied by the P2-Z phase transition [27] and anionic redox [28],

*Contact author: liuh@binghamton.edu

which undermines the energy efficiency. This material also degrades in air [4], posing challenges for material storage and handling. Here, we have successfully synthesized a series of Ca-substituted P2-$Na_xCa_yFe_{0.5}Mn_{0.5}O_2$ materials and examined their electrochemical behavior and stability under exposure to various conditions. Our results show that Ca substitution improves the stability of P2-$Na_xCa_yFe_{0.5}Mn_{0.5}O_2$ under various storage conditions.

II. METHODS

A. Synthesis

P2-$Na_{0.67}Mn_{0.5}Fe_{0.5}O_2$ (NFM) was synthesized by a solid-state reaction as described by Komaba's group [27]: stoichiometric amounts of Na_2O_2 (97%, Sigma), Fe_2O_3 (99.8%, STREM), and Mn_2O_3 (99%, Sigma) were thoroughly mixed and ground in a glovebox (O_2 < 0.5 ppm, H_2O < 0.5 ppm). The mixed powder was pressed into pellets (~ 1 g/pellet), which were then calcined at 960 °C for 12 h in a box furnace (KSL-1200X, MTI) in the air with a heating rate of 3 ℃/min. To quench the pellet to room temperature, the pellet was poured out of the crucible on a thick copper plate (152 mm ×152mm ×26 mm). The glow from the pellet subsided in less than 5 seconds, and the pellet cooled to 30 ~ 40 °C within 1 minute. The pellet was then immediately transferred into the glove box to avoid potential exposure to moisture. The pellet was then ground into powder for storage in the glovebox.

Ca-substitution for Na in NFM followed an ion exchange method reported previously [30]. Firstly, anhydrous $Ca(NO_3)_2$ (by dehydrating $Ca(NO_3)_2{\cdot}4H_2O$ (99.0%, Sigma Aldrich) at 200 °C for 12 h in the air) was mixed with NFM in the desired stoichiometries (i.e., 0.02, 0.05, and 0.07 mol of $Ca(NO_3)_2$ per mol of NFM for the desired stoichiometry of-$Na_xCa_yFe_{0.5}Mn_{0.5}O_2$ with y = 0.02, 0.05, and 0.07, respectively) and pressed to pellets (~ 0.8 g/pellet) in the glovebox. Afterward, the pellets were heated in a tube furnace (STF1200, Across International) for ion exchange reaction at 310 °C (heating rate = 3 ℃/min) with oxygen flow for 48 h. After the ion exchange, the pellets were immediately transferred into the glovebox and ground into fine powder. The powder samples were washed with anhydrous ethanol (200 Proof, Pharmco) three times under an anhydrous environment to remove the nitrates. The washed powder samples were recovered by centrifuging and dried in vacuum before storage in the glovebox.

B. Characterization

X-ray powder diffraction (XRD) was conducted with a Bruker D8 Advance diffractometer in the Bragg-Brentano geometry at room temperature with a dichromatic Mo Kα radiation with 5-55° 2θ. Operando XRD during electrochemical cycling was performed in customized coin cells with the same diffractometer but in transmission geometry. The customized cells were modified from CR2016 cells with rectangular slits (10 mm × 2 mm) sealed with epoxy resin to allow X-ray transmission [31]. Operando XRD for acid dissolution was also conducted in transmission geometry where 10 mg sample was loaded in a sealed plastic vial with 1 mL HCl at pH = 0.9. Phase identification was done with DIFFRAC.EVA V4.0 using the 2025 ICDD database. Rietveld refinement was conducted using TOPAS academic v6 [32].

The POWGEN instrument at the Spallation Neutron Source at Oak Ridge National Laboratory was used to collect neutron powder diffraction (NPD) data. y = 0.07 P2-$Na_xCa_yFe_{0.5}Mn_{0.5}O_2$ was sealed in a vanadium can in an inert atmosphere and was measured under ambient conditions. The sample mass was approximately 1.4 grams and was measured for 1 hour. Frame 1 with a center wavelength of 0.8 Å was used for the measurement.

Inductively coupled plasma optical emission spectrometry (ICP-OES) was conducted with a Varian Vista-MPX Axial ICP-OES for the elemental analysis of NFM and the ion-exchanged samples. In a typical sample preparation for ICP analysis, 4 – 6 mg powder sample was dissolved under stirring in 5.00 mL fresh aqua regia, which was prepared by nitric acid (68 - 70%, ACS Grade, VWR CHEMICALS) and hydrochloric acid (22° Bé, Technical Grade, Fisher Chemical) in 1:3 v/v, with stirring. Once the powders are completely dissolved, the solution was diluted to 200.00 mL, and a 10.00 mL aliquot of the diluted solution was used for ICP analysis.

Scanning electron microscopy (SEM) and Energy Dispersive X-Ray spectroscopy (EDS) were conducted with a scanning electron microscope (Supra 55VP, Zeiss). The EDS (EDAX Octane Elect, U.S.) analysis was conducted with an accelerating voltage of 15 kV and a working distance of 15 mm.

High-angle annular dark-field (HAADF) scanning transmission electron microscopy (STEM) and energy-dispersive X-ray spectroscopy (EDX) analyses were performed using a FEI Talos F200X microscope operated at 200 keV at the Center for Functional Nanomaterials, Brookhaven National Laboratory. For sample preparation, the active particles were manually dispersed using wooden toothpicks to ensure an even distribution. Subsequently, the particles were transferred onto a lacey carbon-coated copper grid via electrostatic attraction to facilitate high-resolution imaging and elemental mapping.

Fourier-transform infrared spectroscopy (FT-IR) was conducted with a Shimadzu IRTracer-100 spectrometer in an attenuated total reflection sample stage (QATR-10).

The PHI 5000 VersaProbe II (Japan) with an aluminum anode was used for X-ray photoelectron spectroscopy (XPS) with 15 kV anode voltage and 50 W power. The graphitic carbon 1 s peak at 284.5 eV was used as the calibration standard for the measured XPS spectra.

C. Electrochemistry

All electrochemical measurements were conducted with 2032 coin cells. Composite cathodes were fabricated by pressing a mixture of 60 wt% active materials (AM), 20 wt% carbon black (acetylene, 99.9+ %, Alfa Aesar) and 20 wt% poly(vinylidene fluoride) (PVDF) (M_w ~534000, Sigma Aldrich) into pellets in the glovebox, leading to an area loading of 17-20 mg/cm^2 AM. Sodium metal (99.8%, Sigma) was used as the anode, 1.0 M $NaPF_6$ in propylene carbonate (PC) with 5 vol % fluorinated ethylene carbonate (Gotion) was used as the electrolyte, and the glass fiber filters (Whatman) were used as separators. Galvanostatic cycling of the cells was conducted using a battery testing system (LAND) in the voltage window of 1.5 – 4.3 V at room temperature. The specific current was calculated based on the theoretical capacity of 262 mAh/g.

III. RESULTS

A. Ca substitution for Na in P2-$Na_{0.67}Fe_{0.5}Mn_{0.5}O_2$ via ion exchange

Fig 1a shows the XRD patterns of the Ca-substituted $Na_xCa_yFe_{0.5}Mn_{0.5}O_2$ samples obtained through ion exchange with the P2-$Na_{0.67}Fe_{0.5}Mn_{0.5}O_2$ (see **Fig S1** for the Rietveld refinement profile for the y = 0 P2-$Na_xCa_yFe_{0.5}Mn_{0.5}O_2$ [33]). All Ca-substituted samples maintain the same P2 phase as the parent P2-$Na_{0.67}Fe_{0.5}Mn_{0.5}O_2$ material. The y = 0 sample corresponds to the sample that underwent the same thermal treatment as the ion exchange experiment without mixing any nitrate salt and serves as the control sample. A noticeable shift in the peak position is observed for the y = 0 sample, which indicates changes in the P2 phase during the ion exchange experiment even in the absence of Ca substitution. This is attributed to the oxidation of $Na_{0.67}Fe_{0.5}Mn_{0.5}O_2$ by pure O_2 gas at elevated temperatures (see **Fig S2** for the XRD patterns for the as-synthesized P2-$Na_{0.67}Fe_{0.5}Mn_{0.5}O_2$ sample after annealing in pure oxygen gas [33]). As y increases, all peaks systemically shift to higher angles, which are represented by the shift of the (004) and (100) reflections to higher angles, respectively (**Fig 1b**). The refined unit cell parameters all decrease with increasing y (**Fig 1c**), indicating successful Ca substitution. Attempts to directly synthesize Ca-substituted P2-$Na_xCa_yFe_{0.5}Mn_{0.5}O_2$ via the solid -state method did not yield phase-pure product, likely caused by the instability of the substituted phases at high temperature (see **Fig S3** for XRD patterns of the direct solid-state synthesis product and the high-temperature annealed y = 0.07 sample [33]).

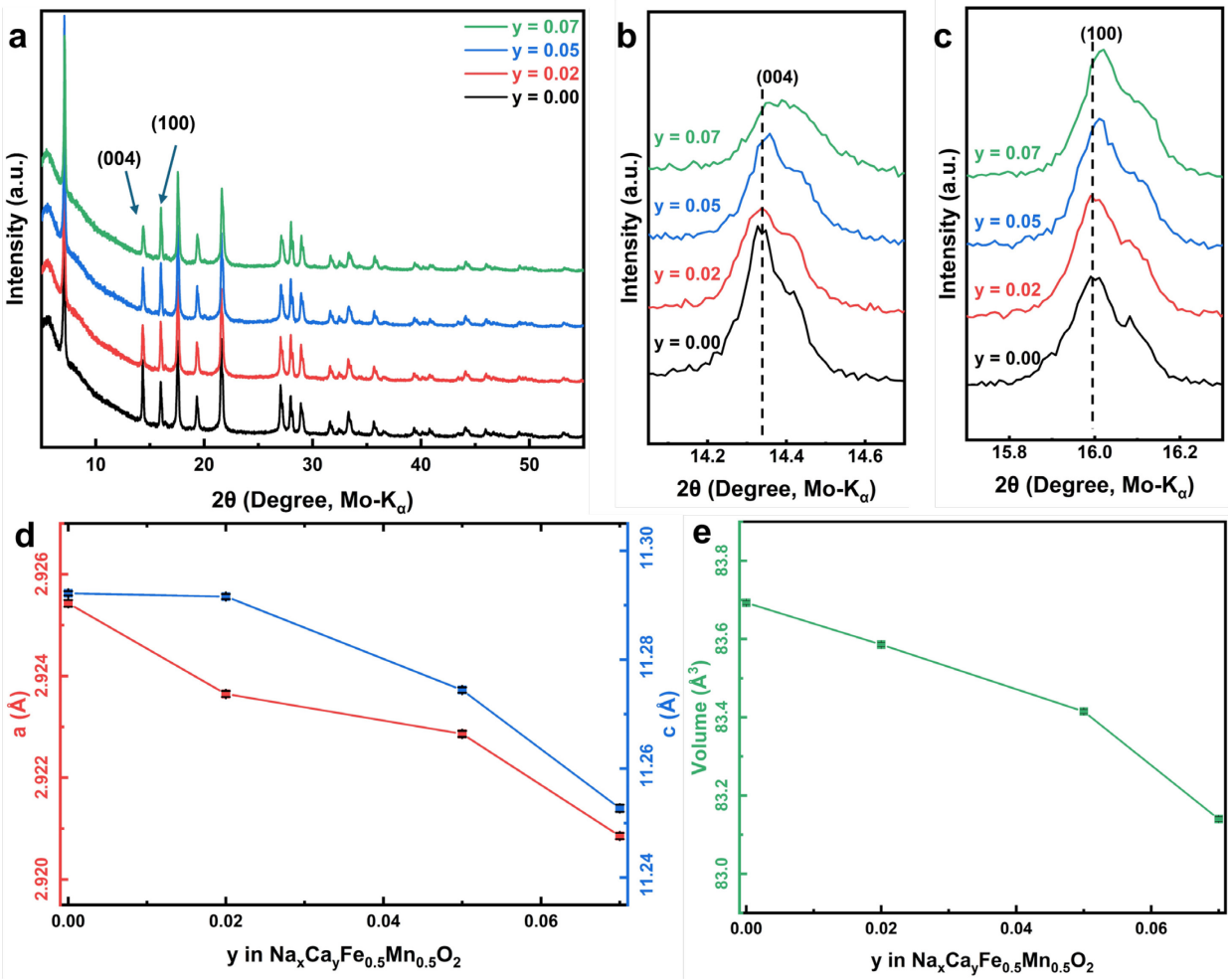

FIG 1. (a-c) XRD patterns measured for P2-$Na_xCa_yFe_{0.5}Mn_{0.5}O_2$ (y = 0.00, 0.02, 0.05, and 0.07), and (d-e) refined lattice parameters.

Elemental analysis was conducted to confirm the incorporation of Ca in the ion-exchanged samples. The ICP result reveals a decreasing Na composition (x) with increasing Ca composition (y) for all ion-exchange samples (**Fig 2**). A linear regression analysis of x and y for all ion-exchanged samples shows that the increment of 1 Ca is accompanied by the decrement of 2 Na, which is consistent with the charge balance expected for the exchange of 2 monovalent Na^+ ions for 1 divalent Ca^{2+} ion. This demonstrates that the ion exchange reaction successfully substitutes Na cations with Ca cations in the desired stoichiometry. The EDS mapping result shows that Ca uniformly distributes among particles in the y = 0.07 sample (**Fig 3**, see **Fig S4** for additional images [33]), which validates Ca substitution in the bulk of the crystal lattice.

To determine the crystallographic occupation of Ca in the substituted phases, Rietveld refinement was conducted simultaneously against the neutron and X-ray powder diffraction patterns measured for the y = 0.07 sample (see **Fig S5** and **Table. S1** for the combined XRD and NPD refienment result [33]). Constraining the total Na and Ca occupancies to the ICP values was necessary to break the high correlation between the refined Ca and Na ocupancies. The refinement result shows that all Ca ions occupies the edge-sharing site, which is the more stable site due to the longer separation from transition metal cations.

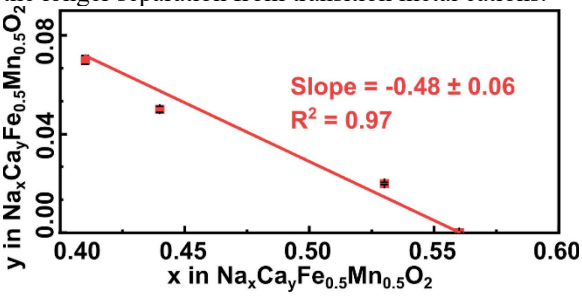

FIG 2. Elemental composition of Ca (y) vs. Na (x) measured for P2-$Na_xCa_yFe_{0.5}Mn_{0.5}O_2$ by ICP. Red line corresponds to the linear fitting.

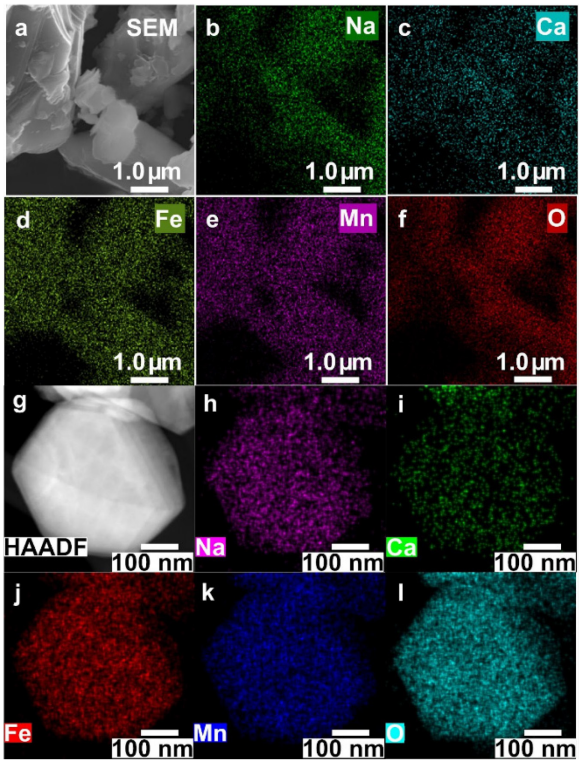

FIG 3. (a-f) SEM image and corresponding EDS elemental maps and (g-l) HAADF-STEM image and corresponding EDS elemental maps of the y = 0.07 P2-$Na_xCa_yFe_{0.5}Mn_{0.5}O_2$ particles.

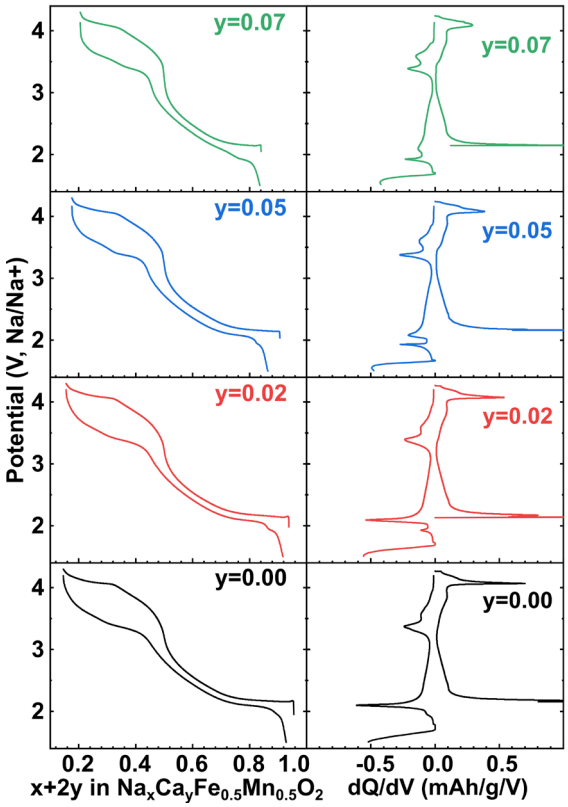

FIG 4. Voltage profile measured for the first full galvanostatic cycling of P2-$Na_xCa_yFe_{0.5}Mn_{0.5}O_2$ (y = 0.00, 0.02, 0.05, and 0.07) at 13 mA/g (C/20), 1.5 V - 4.3 V and the corresponding differential capacity (dQ/dV) plot.

B. Electrochemical behavior of P2-$Na_xCa_yFe_{0.5}Mn_{0.5}O_2$

Galvanostatic cycling was used to characterize the electrochemical behavior of the $Na_xCa_yFe_{0.5}Mn_{0.5}O_2$. **Fig 4** shows the voltage profile and the differential capacity (dQ/dV) curve for the first full cycle between 1.5 V and 4.3 V following the initial discharge to 1.5 V at C/20 (13 mA/g). All samples exhibit the characteristic voltage profile of the P2-$Na_{0.67}Fe_{0.5}Mn_{0.5}O_2$: a reversible slopy voltage profile below 3.2 V, which corresponds to the Mn^{4+}/Mn^{3+} redox reaction, and a large voltage hysteresis above 3.2 V, which has been attributed to the partial oxidation of Fe^{3+} and the anionic redox of lattice oxygen [26,34]. The dQ/dV peaks for the P2-Z phase transition at 4.06 V and the P2-P'2 phase transition at 2.10 V attenuate with increasing y, suggesting a suppression of these phase transitions with Ca substitution. For the y = 0 sample, the discharge capacity is 0.80 Na per formula unit (f.u.) of $Na_xCa_yFe_{0.5}Mn_{0.5}O_2$ at C/20 (equivalent to 210 mAh/g at 13 mA/g), which is slightly higher than the reported value of 200 mAh/g [4]. As y increases to 0.07, the reversible capacity decreases to 0.65 Na per f.u. (equivalent to 170 mAh/g) (**Fig 4**). This capacity loss with Ca substitution is comparable with other Ca-substituted sodium layered transition metal oxide cathode materials [20,21,23–25] (see **Fig S6** for comparison with reported Ca-substituted materials [33]). A loss in capacity is observed for both the high-voltage (> 3.2 V) and the low-voltage (< 3.2 V) regimes (**Fig 5**). The high-voltage capacity loss suggests that Ca^{2+} ions are immobile and do not de-intercalate at the end of charge, and Ca substitution partially deactivates both the Fe and anionic redox activities, which is expected for substitution at the Na site. The capacity loss in the low-voltage regime is puzzling since the aliovalent substitution by Ca introduces additional vacancies at intercalation sites. A recent study of Ca-substituted O3-$NaNi_{1/3}Fe_{1/3}Mn_{1/3}O_2$ also reported a decreased capacity in the low voltage regime [25]. To examine the cause of the reduced capacity, synchrotron XRD was measured for the y = 0 and 0.07 electrode samples recovered from the end of discharge at 1.5 V (**Fig 6**). Both the P2 and the distorted P'2 phases are observed at the end of discharge, consistent with the previous operando XRD study of the phase transition during electrochemical cycling of $Na_xFe_{0.5}Mn_{0.5}O_2$ [26] The refined weight fraction of the P'2 phase in the y = 0 sample is 64.2 %, which is higher than 54.6 % in the y

= 0.07 sample (refined parameters given in **Table S2** [33]). Therefore, Ca substitution retards the P2-to-P'2 phase transition upon Na intercalation and explains the decreased capacity observed for the low-voltage regime in Ca-substituted samples.

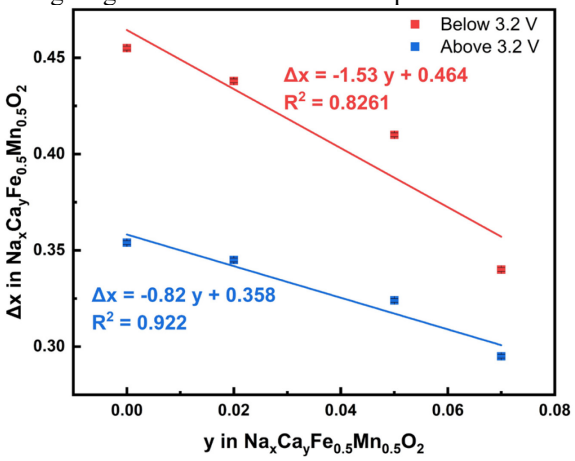

FIG 5. Number of intercalated Na (Δx) per formula unit of $Na_xCa_yFe_{0.5}Mn_{0.5}O_2$ for y = 0.00, 0.02, 0.05, and 0.07 in the voltage windows below and above 3.2 V.

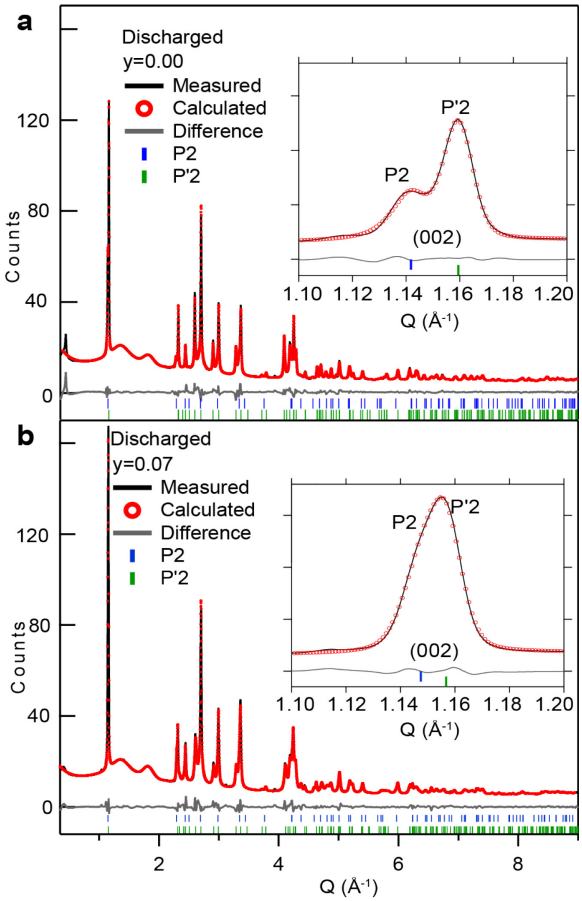

FIG 6. Synchrotron XRD measured for the (a) y = 0 and (b) y = 0.07 P2-$Na_xCa_yFe_{0.5}Mn_{0.5}O_2$ electrode samples discharged to 1.5 V.

The long-term cycling performance was evaluated in 1.5 – 4.3 V at the C/20 rate (**Fig 7**). The y = 0 sample outperforms all the substituted samples in capacity retention. A comparison between the substituted samples does not show any relationship between capacity retention and Ca substitution. The y = 0 sample also outperforms the as-synthesized $Na_{0.67}Fe_{0.5}Mn_{0.5}O_2$ sample up to 50 cycles.

C. Ca pillar effect on phase transitions.

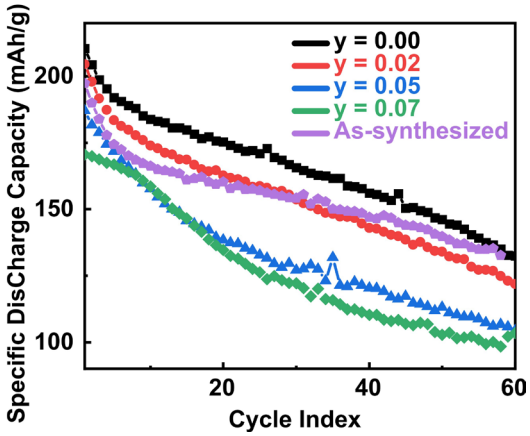

FIG 7. The discharge capacity degradation of P2-$Na_xCa_yFe_{0.5}Mn_{0.5}O_2$ (y = 0.00, 0.02, 0.05, and 0.07) and the as-synthesized $Na_{0.67}Fe_{0.5}Mn_{0.5}O_2$ electrode samples at 13 mA/g (C/20), 1.5 – 4.3 V.

To determine the effect of Ca pillars on the structural phase transitions during electrochemical cycling, laboratory operando XRD was measured for the y = 0 and y = 0.07 samples for the full charge-discharge cycle following an initial discharge to 1.5 V(**Fig 8**). For the non-substituted y = 0 sample (**Fig 8a**), the P'2-P2 phase transition at the beginning of charge is well resolved by the appearance of the (002) reflection for the P2 phase at the expense of the reflection for the P'2 phase. Following this phase transition, the (002) reflection continuously shifts to a lower angle until 4.06 V, where it starts to shift to a higher angle and attenuates in intensity. This change in the shift direction is accompanied with the appearance of the (002) reflection of the Z phase. The Z (002) reflection continues to shift to a higher angle until the end of charge. This phase evolution process is mirrored on discharge. This operando XRD result is consistent with previous operando XRD result reported for the P2-$Na_{0.67}Fe_{0.5}Mn_{0.5}O_2$ [26].

For the y = 0.07 sample (**Fig 8b**), only a single reflection is observed during the charge process until the appearance of the Z phase at 4.03 V. The failure to

observe the P'2-P2 phase transition at the beginning of charge is ascribed to the limited resolution of the instrument to resolve the reduced lattice difference between the two phases, which is evident in the asymmetric peak profile of the (002) reflection in the *ex situ* synchrotron XRD result shown in **Fig 6b**. Hence, the Ca pillar reduces the lattice mismatch between the P'2 and P2 phases. The (002) reflection intensity appears to evolve smoothly between the P2 and the Z phases, indicating also a reduced lattice mismatch between the two phases.

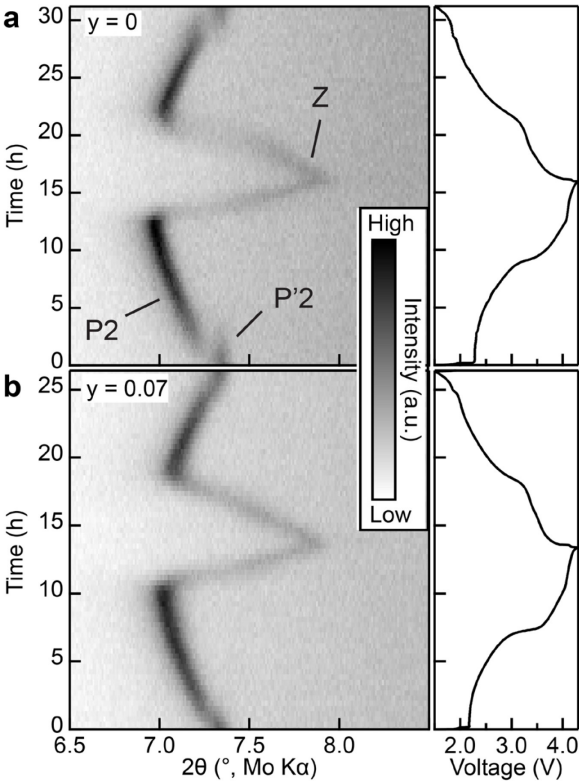

FIG 8. Operando XRD measurement of the (002) reflection for (a) y = 0 and (b) y = 0.07 cathode materials during the first full charge-discharge cycle between 1.5 V and 4.3 V.

Profile fitting of the operando XRD patterns was used to determine the unit cell parameters of the P2 and Z phases during cycling (**Fig 9**). The lattice mismatch between the two phases is most pronounced in the *c* lattice during discharge. At any given time during the Z-P2 phase transition, the difference in the *c* lattice parameter is in the range of 0.38 – 0.70 Å for the y = 0 sample, but is significantly reduced to the range of 0.24 – 0.36 Å for the y = 0.07 sample. This result again demonstrates the Ca pillaring effect on relieving the lattice mismatch during structural phase transitions.

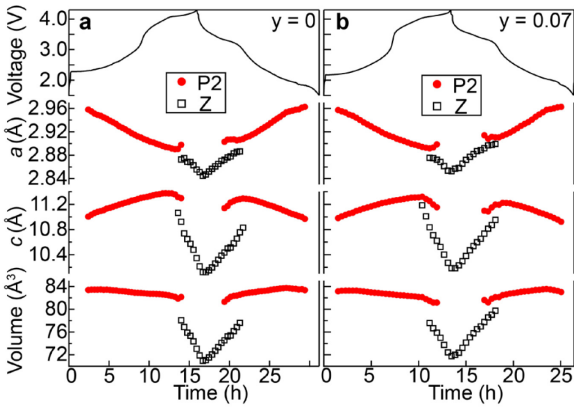

FIG 9. Refined unit cell parameters of the P2 and Z phases for (a) y =0 and (b) y = 0.07 samples in a full charge-discharge cycle.

D. Stability of P2-$Na_xCa_yFe_{0.5}Mn_{0.5}O_2$ under air, moist CO_2, and water.

To examine the stability of the Ca-substituted samples, XRD measurement was performed for $Na_xCa_yFe_{0.5}Mn_{0.5}O_2$ (y = 0.00, 0.02, 0.05, and 0.07) samples after being exposed in air for 48 h (humidity = 50 - 60%), deionized water for 24 h, or moist CO_2 surrounding for and 48 h (humidity = 80 - 90%, flow rate = 80.0 mL/min) (**Fig 10**).

For 48 h air exposure, the XRD patterns measured for all samples do not show any significant differences from the pristine (i.e., non-exposed) samples (**Fig 10a**). This is consistent with a previous study on the stability of the P2-$Na_{0.67}Fe_{0.5}Mn_{0.5}O_2$, where additional Bragg peaks are observed only after a week of air exposure [4].

For water soaking, only the y = 0 sample shows a broad shoulder at the lower-angle side of the (002) reflection of the P2 phase (**Fig 10b**), which has been reported for a week-long air-exposed sample [4]. No new peaks are observed for the Ca-substituted samples (y = 0.02, 0.05, and 0.07), demonstrating the positive role of Ca substitution in stabilizing $Na_xCa_yFe_{0.5}Mn_{0.5}O_2$ against exposure to water.

For moist CO_2 exposure, a new low-angle peak emerges at 5.75° 2θ (*d*-spacing = 7.06 Å) and has been previously assigned to a hydrated phase [4]. This intercalated layered phase also explains a few other newly emerged peaks at higher angles (**Fig 10c**). The group of new peaks observed at 13.2°, 13.8°, and 15.6° 2θ can be assigned to $NaHCO_3$, which is cross-validated by FTIR (**Fig S7** [33]). This is consistent with a previous report that moist CO_2 leads to $NaHCO_3$ formation via Na^+/H^+ ion exchange [5]. The relative intensity of the peaks corresponding to the intercalated layered phase decreases with increasing y,

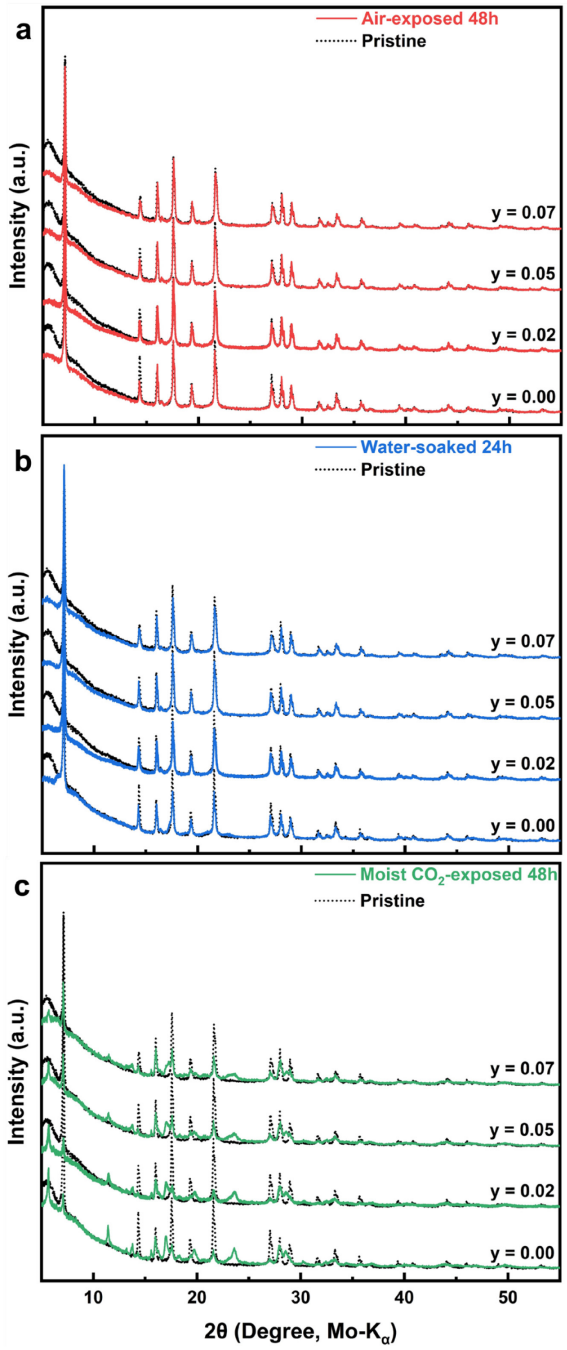

FIG 10. XRD patterns of P2-$Na_xCa_yFe_{0.5}Mn_{0.5}O_2$ (y = 0.00, 0.02, 0.05, and 0.07) before and after air, water, and moist CO_2, exposure.

demonstrating the role of Ca substitution in slowing down the kinetics of the deleterious side reactions with moist CO_2. The X-ray photoelectron spectra of O 1s measured for the y = 0 and 0.07 samples show a decreased contribution from the transition metal oxide lattice for the y = 0 sample (**Fig S8** [33]), further confirming the increased stability of the y = 0.07 sample exposed to moist CO_2.

Galvanostatic cycling was performed for all exposed samples in the voltage window of 1.5 – 4.3 V at C/20. **Fig 11** shows the voltage profile for the first charge-discharge cycles. The voltage profile for the air-exposed samples does not show a significant difference from the unexposed samples, which is consistent with the lack of change in the XRD result after air exposure (**Fig 10a**). Water soaking induces an increased voltage polarization for y = 0, 0.02, and 0.05 samples but not as much for the y = 0.07 sample. Moist CO_2 exposure resulted in the largest increase in the voltage polarization, consistent with the degradation of the P2-$Na_xCa_yFe_{0.5}Mn_{0.5}O_2$ phase observed in the XRD result **(Fig 10c).**

The long-term cycling stability for the exposed samples is shown in **Fig 12**. For both the air-exposed and water-soaked samples, the y = 0 sample outperforms all the Ca-substituted samples. While the y = 0.02 sample has higher capacity than both the y = 0.05 and 0.07 samples, there is no significant difference between the y = 0.05 and 0.07 samples. For moist-CO_2-exposed samples, the cycling stability increases with increasing Ca substitution, which is consistent with the decreased fraction of the hydrated phase with increasing Ca substitution.

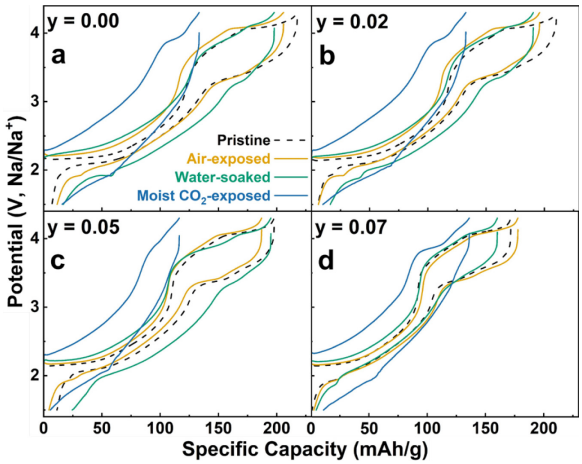

FIG 11. The comparison of the first full charge-discharge cycled curves of P2-$Na_xCa_yFe_{0.5}Mn_{0.5}O_2$ (a) y = 0.00, (b) y = 0.02, (c) y = 0.05, and (d) y = 0.07 between pristine and after exposure at 13 mA/g (C/20), 1.5 – 4.3 V.

IV. DISCUSSION

Ca substitution at the Na site can be challenging when the Ca-rich end-member phase of the $Na_{x-2y}Ca_yMO_2$ (M = transition metal ion) solid solution series is not stable. Therefore, direct substitution via the conventional solid-state synthesis method may not be viable. To the best of our knowledge, neither Ca_yMnO_2 nor

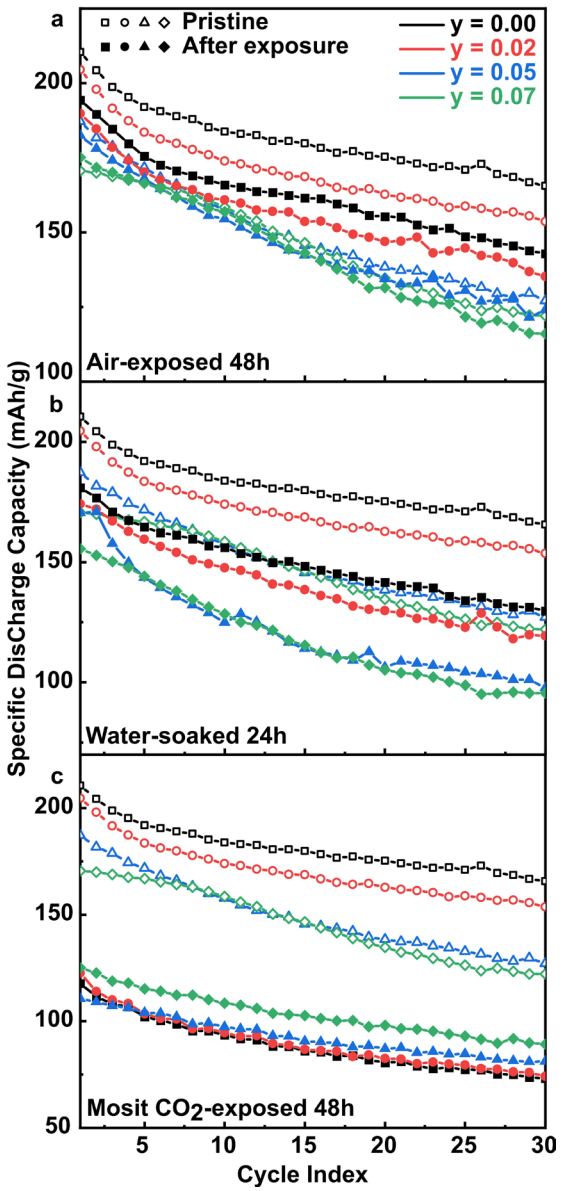

FIG 12. Specific discharge capacity measured for (a) air-exposed, (b) water-soaked, and (c) moist CO_2-exposed P2-$Na_xCa_yFe_{0.5}Mn_{0.5}O_2$ samples at 13 mA/g (C/20), 1.5 – 4.3 V.

Ca_yFeO_2 has been reported experimentally to form in the layered phase, although density functional theory calculations predict a small energy above the hull for $Ca_{0.5}MnO_2$ and $Ca_{0.5}FeO_2$ [35], suggesting possible stabilization of these phases using metastable synthesis techniques. Although Ca doping at low concentrations (1~2%) via solid-state methods has been reported for $Na_{1-2y}Ca_yNi_{1/2}Mn_{1/2}O_2$ [23], and $Na_{1-2y}Ca_yNi_{1/3}Fe_{1/3}Mn_{1/3}O_2$ [22], impurity phases are readily observed for $y \geq 0.02$. This raises the possibility that impurity phases are also present for $y < 0.02$ but remain unresolved due to experimental limitations. Therefore, ion exchange provides a general method for Ca substitution at the Na site when the Ca-containing phase is metastable. On the other hand, when the Ca-rich end-member phase is stable, a complete solid solution between the Na- and Ca-containing phases can be realized. For example, the presence of the thermodynamically stable layered $Ca_{0.5}CoO_2$ phase [36] allows for the solid-state synthesis of the $Na_xCa_yCoO_2$ solid solution series [20,37].

The improved stability of $Na_xCa_yFe_{0.5}Mn_{0.5}O_2$ under various exposure conditions agrees with previous studies on Ca-doped sodium layered transition metal oxides [24,25]. This is likely attributed to the higher equivalent bond enthalpies of Ca (558 kJ/mol) than Na (523 kJ/mol) in ternary oxides [29]. Previous studies on air stability of sodium layered transition metal oxides proposed the H^+/Na^+ ion exchange as a precursor to the subsequent hydration and layer expansion [5]. Hence, the stronger Ca-O bond and the low mobility of Ca^{2+} ions in layered oxides likely hinder this ion exchange process. Indeed, Ca substitution impedes the hydration kinetics of $Na_xCa_yFe_{0.5}Mn_{0.5}O_2$ in acidic solutions, and the layered phase remains effectively stable for high levels of Ca substitution ($y = 0.5$), demonstrating the stability of Ca^{2+} against ion exchange with H^+ (see **Fig S9** for the operando XRD results of $Na_xCa_yFe_{0.5}Mn_{0.5}O_2$ dissolution in acids [33]).

Unlike previous studies that all reported improved cycling stability for Ca-substituted samples [24,25,37–39], our work does not show improvement with Ca substitution for $Na_xCa_yFe_{0.5}Mn_{0.5}O_2$ despite the observed pillaring effect that reduces the lattice mismatch during phase transitions. Previous work has identified the primary cause of the capacity fade to be the P2-Z phase transition [26], which involves both a lattice mismatch and the transition metal migration to the tetrahedral sites in the alkaline layer in the formation of the Z phase. It is remarkable that the volume difference between the P2 and Z phase for the $y = 0$ phase is in the range of 6% – 8%, which is significantly smaller than the 20% difference between the P2 and O2 phases reported for the Ni and Mn-based layered oxide materials [40,41]. Hence, lattice mismatch may not be the predominant cause of the capacity face. The other mechanism that drives the capacity fade is the transition metal migration to the alkaline ion layer in the Z phase. The substitution of Na by Ca increases the vacancy concentration in the alkaline ion layer, which creates a conducive environment for transition metal migration. It is likely that Ca pillaring aggravates the transition metal migration during the P2-Z phase transition, undermining the long-term cycling stability.

V. CONCLUSIONS

Ion exchange proves an effective method for Ca substitution at the Na site in the P2-$Na_xCa_yFe_{0.5}Mn_{0.5}O_2$. Despite the beneficial effect of reduced lattice mismatch during the P2-P'2 and P2-Z phase transitions, the incorporation of Ca in the Na layer decreases the reversible capacity of the P2-$Na_xCa_yFe_{0.5}Mn_{0.5}O_2$ with no significant improvement in the long-term capacity degradation. Nevertheless, the stability of the P2-$Na_xCa_yFe_{0.5}Mn_{0.5}O_2$ under various storage conditions increases with increasing Ca substitution. This work demonstrates the intriguing effect of cationic substitution at the Na site, which deserves further investigation to harness the pillar effect.

ACKNOWLEDGMENT

This work was supported by the National Science Foundation CBET-2144296. This research used beamline 28-ID-2 (proposal number 317372) at the National Synchrotron Light Source II, a U.S. Department of Energy (DOE) Office of Science User Facility operated for the DOE Office of Science by Brookhaven National Laboratory under Contract No. DE-SC0012704. A portion of this research used resources at the Spallation Neutron Source, a DOE Office of Science User Facility operated by the Oak Ridge National Laboratory. The beam time was allocated to BL-11A (POWGEN) on proposal number IPTS-36257.1. The research also used the electron microscopy facilities of the Center for Functional Nanomaterials, which is a U.S. DOE Office of Science Facility at Brookhaven National Laboratory under Contract No. DE-SC0012704. L.Q. and G.Z. acknowledge support from the U.S. Department of Energy, Office of Basic Energy Sciences, Division of Materials Sciences and Engineering, under Award No. DE-SC0001135.

DATA AVAILABILITY

The data that support the findings of this article are openly available [42]

[1] N. Yabuuchi, K. Kubota, M. Dahbi, and S. Komaba, Research Development on Sodium-Ion Batteries, Chem. Rev. **114**, 11636 (2014).

[2] X. Xiang, K. Zhang, and J. Chen, Recent Advances and Prospects of Cathode Materials for Sodium-Ion Batteries, Adv. Mater. **27**, 5343 (2015).

[3] W. Zuo et al., The stability of P2-layered sodium transition metal oxides in ambient atmospheres, Nat. Commun. **11**, 3544 (2020).

[4] V. Duffort, E. Talaie, R. Black, and L. F. Nazar, Uptake of CO2 in Layered P2-Na0.67Mn0.5Fe0.5O2: Insertion of Carbonate Anions, Chem. Mater. **27**, 2515 (2015).

[5] Y. Yang et al., Decoupling the air sensitivity of Na-layered oxides, Science **385**, 744 (2024).

[6] Y.-S. Hu and Y. Li, Unlocking Sustainable Na-Ion Batteries into Industry, ACS Energy Lett. **6**, 4115 (2021).

[7] Y. Li et al., Degradation by Kinking in Layered Cathode Materials, ACS Energy Lett. **6**, 3960 (2021).

[8] K. Wang, P. Yan, and M. Sui, Phase transition induced cracking plaguing layered cathode for sodium-ion battery, Nano Energy **54**, 148 (2018).

[9] E. Gabriel et al., Influence of Interlayer Cation Ordering on Na Transport in P2-Type Na0.67–xLiy Ni0.33–zMn0.67+zO2 for Sodium-Ion Batteries, J. Am. Chem. Soc. **146**, 15108 (2024).

[10] E. de la Llave et al., Improving Energy Density and Structural Stability of Manganese Oxide Cathodes for Na-Ion Batteries by Structural Lithium Substitution, Chem. Mater. **28**, 9064 (2016).

[11] L. Yang et al., Lithium-Doping Stabilized High-Performance P2–Na0.66Li0.18Fe0.12Mn0.7O2 Cathode for Sodium Ion Batteries, J. Am. Chem. Soc. **141**, 6680 (2019).

[12] S. Mariyappan, T. Marchandier, F. Rabuel, A. Iadecola, G. Rousse, A. V. Morozov, A. M. Abakumov, and J.-M. Tarascon, The Role of Divalent (Zn2+/Mg2+/Cu2+) Substituents in Achieving Full Capacity of Sodium

Layered Oxides for Na-Ion Battery Applications, Chem. Mater. **32**, 1657 (2020).
[13] F. Ding, C. Zhao, D. Xiao, X. Rong, H. Wang, Y. Li, Y. Yang, Y. Lu, and Y.-S. Hu, Using High-Entropy Configuration Strategy to Design Na-Ion Layered Oxide Cathodes with Superior Electrochemical Performance and Thermal Stability, J. Am. Chem. Soc. **144**, 8286 (2022).
[14] Q. Wang, Y.-S. Hu, H. Li, H.-M. Cheng, T. Zhao, and C. Zhao, Ionic potential for battery materials, Nat. Rev. Mater. 1 (2025).
[15] *Rational Design of Layered Oxide Materials for Sodium-Ion Batteries | Science*, https://www.science.org/doi/10.1126/science.aay9972.
[16] M. A. Kim, E. K. Zimmerer, Z. T. Piontkowski, M. A. Rodriguez, N. B. Schorr, B. R. Wygant, J. S. Okasinski, A. C. Chuang, T. N. Lambert, and J. W. Gallaway, Li-ion and Na-ion intercalation in layered MnO2 cathodes enabled by using bismuth as a cation pillar, J. Mater. Chem. A **11**, 11272 (2023).
[17] Y. Wang et al., Pillar-beam structures prevent layered cathode materials from destructive phase transitions, Nat. Commun. **12**, 13 (2021).
[18] G. T. Hill, F. Shi, H. Zhou, Y. Han, and C. Liu, Layer spacing gradient (NaLi)1−xCoO2 for electrochemical Li extraction, Matter **4**, 1611 (2021).
[19] C. Heubner, B. Matthey, T. Lein, F. Wolke, T. Liebmann, C. Lämmel, M. Schneider, M. Herrmann, and A. Michaelis, Insights into the electrochemical Li/Na-exchange in layered LiCoO2 cathode material, Energy Storage Mater. **27**, 377 (2020).
[20] M. Matsui, F. Mizukoshi, and N. Imanishi, Improved cycling performance of P2-type layered sodium cobalt oxide by calcium substitution, J. Power Sources **280**, 205 (2015).
[21] Y. Ishado, H. Hasegawa, S. Okada, M. Mizuhata, H. Maki, and M. Matsui, An experimental and first-principle investigation of the Ca-substitution effect on P3-type layered NaxCoO2, Chem. Commun. **56**, 8107 (2020).
[22] L. Zhang, J. Deshmukh, H. Hijazi, Z. Ye, M. B. Johnson, A. George, J. R. Dahn, and M. Metzger, Impact of Calcium on Air Stability of Na[Ni1/3Fe1/3Mn1/3]O2 Positive Electrode Material for Sodium-ion Batteries, J. Electrochem. Soc. **170**, 070514 (2023).
[23] T.-Y. Yu, J. Kim, J.-Y. Hwang, H. Kim, G. Han, H.-G. Jung, and Y.-K. Sun, High-energy O3-Na1−2xCax[Ni0.5Mn0.5]O2 cathodes for long-life sodium-ion batteries, J. Mater. Chem. A **8**, 13776 (2020).
[24] L. Zheng, J. C. Bennett, and M. N. Obrovac, Stabilizing NaCrO2 by Sodium Site Doping with Calcium, J. Electrochem. Soc. **166**, A2058 (2019).
[25] W. Li et al., Navigating low state of charge phase transitions in layered cathodes for long-life sodium-ion batteries, Energy Environ. Sci. **18**, 6032 (2025).
[26] E. Talaie, V. Duffort, H. L. Smith, B. Fultz, and L. F. Nazar, Structure of the high voltage phase of layered P2-Na2/3−z[Mn1/2Fe1/2]O2 and the positive effect of Ni substitution on its stability, Energy Environ. Sci. **8**, 2512 (2015).
[27] N. Yabuuchi, M. Kajiyama, J. Iwatate, H. Nishikawa, S. Hitomi, R. Okuyama, R. Usui, Y. Yamada, and S. Komaba, P2-type Nax[Fe1/2Mn1/2]O2 made from earth-abundant elements for rechargeable Na batteries, Nat. Mater. **11**, 512 (2012).
[28] *Controlling Iron Versus Oxygen Redox in the Layered Cathode Na0.67Fe0.5Mn0.5O2: Mitigating Voltage and Capacity Fade by Mg Substitution - Boivin - 2022 - Advanced Energy Materials - Wiley Online Library*,

https://advanced.onlinelibrary.wiley.com/doi/full/10.1002/aenm.202200702.

[29] M. O'Keeffe and J. A. Stuart, Bond energies in solid oxides, Inorg. Chem. **22**, 177 (1983).

[30] B. L. Cushing and J. B. Wiley, Topotactic Routes to Layered Calcium Cobalt Oxides, J. Solid State Chem. **141**, 385 (1998).

[31] F. Niu, L. Qiao, H. Huang, E. A. Odero, G. Zhou, and H. Liu, Is surface modification effective to stabilize high-voltage cycling for layered P2-Na $_{2/3}$ Ni $_{1/3}$ Mn $_{2/3}$ O $_{2}$ cathodes?, Chem. Commun. 10.1039.D4CC02819H (2024).

[32] A. A. Coelho, TOPAS and TOPAS-Academic: an optimization program integrating computer algebra and crystallographic objects written in C++, J. Appl. Crystallogr. **51**, 210 (2018).

[33] See Supplemental Material at [URL will be inserted by publisher], containing the Rietveld refinement profile for the y = 0 P2-NaxCayFe0.5Mn0.5O2, the comparison of the crystallology between the as-synthesized P2-Na0.67Fe0.5Mn0.5O2 sample and the as-synthesized annealed under pure oxygen gas, XRD patterns of the direct solid-state synthesis product and the high-temperature annealed y = 0.07 sample, the additional TEM and EDS mappings of y = 0.07 sample, the Rietveld refinement profiles of the XRD and NPD, the capacity loss phenomena of this stady and some othe reported Ca substituted cathode materials, FTIR identification for the before and after exposure, the oxidation status of y = 0 and 0.07 samples, the operando XRD patterns of the dissolution in acids, the refined structure parameters based on XRD and NPD, and the refined unit cell parameters of the P2 and P'2 phases at the end of discharge for the y = 0 and 0.07 samples., (n.d.).

[34] F. Li, R. Liu, J. Liu, and H. Li, Voltage Hysteresis in Transition Metal Oxide Cathodes for Li/Na-Ion Batteries, Adv. Funct. Mater. **33**, 2300602 (2023).

[35] H. Park, C. J. Bartel, G. Ceder, and P. Zapol, Layered Transition Metal Oxides as Ca Intercalation Cathodes: A Systematic First-Principles Evaluation, Adv. Energy Mater. **11**, 2101698 (2021).

[36] M. Cabello, F. Nacimiento, J. R. González, G. Ortiz, R. Alcántara, P. Lavela, C. Pérez-Vicente, and J. L. Tirado, Advancing towards a veritable calcium-ion battery: CaCo2O4 positive electrode material, Electrochem. Commun. **67**, 59 (2016).

[37] H. Hasegawa, Y. Ishado, S. Okada, M. Mizuhata, H. Maki, and M. Matsui, Stabilized Phase Transition Process of Layered NaxCoO2 via Ca-Substitution, J. Electrochem. Soc. **168**, 010509 (2021).

[38] L. Sun et al., Insight into Ca-Substitution Effects on O3-Type NaNi1/3Fe1/3Mn1/3O2 Cathode Materials for Sodium-Ion Batteries Application, Small **14**, 1704523 (2018).

[39] S. C. Han, H. Lim, J. Jeong, D. Ahn, W. B. Park, K.-S. Sohn, and M. Pyo, Ca-doped NaxCoO2 for improved cyclability in sodium ion batteries, J. Power Sources **277**, 9 (2015).

[40] K. Kubota, T. Asari, and S. Komaba, Impact of Ti and Zn Dual-Substitution in P2 Type Na2/3Ni1/3Mn2/3O2 on Ni–Mn and Na-Vacancy Ordering and Electrochemical Properties, Adv. Mater. **35**, 2300714 (2023).

[41] Z. Cheng et al., Mitigating the Large-Volume Phase Transition of P2-Type Cathodes by Synergetic Effect of Multiple Ions for Improved Sodium-Ion Batteries, Adv. Energy Mater. **12**, 2103461 (2022).

[42] *Data for "Ca Pillar Effect on the Electrochemistry and Stability of P2-NaxCayFe0.5Mn0.5O2 for Sodium-Ion*

Batteries,"
https://doi.org/10.6084/m9.figshare.301
89877.